CFD SIMULATION ON THERMAL COMFORT IN A LIBRARY BUILDING IN THE TROPICS

Y.H. Yau*, N.N.N. Ghazali, A. Badarudin and F.C. Goh
Department of Mechanical Engineering,
University of Malaya, 50603 Kuala Lumpur, Malaysia.
Corresponding email: yhyau@um.edu.my

Abstract. This paper presents a three-dimensional analysis for thermal comfort in a library. The room model includes library layout, equipment and peripheral positions as well as the positions of inlet and outlet air for IAQ controls. Cold clean air is supplied to the room through ceiling-mounted air grilles and exhausted through air grilles situated on the same ceiling. A commercial CFD package was used in this study to achieve solutions of the distribution of airflow velocity and temperature. Using high quality meshes is vital to the overall accuracy of the results. Simulation results show a good agreement with experimental data from the literature. This study has thoroughly analysed the indoor thermal conditions and airflow characteristics of the building. In addition, verification of the CFD program with experimental data showed that the program can provide reasonable and reliable predictions on thermal comfort performance with the help of precise boundary conditions.

Keywords: CFD, FLUENT, thermal comfort, IAQ, library, HVAC
PACS: 47.11.-j

1. INTRODUCTION

Air conditioning is usually applied to impart a cooling effect. However, air conditioning, by definition, requires six functions to take place. These six functions are cooling, heating, air circulation, air cleaning, humidification, and dehumidification. When the system is operating in the cooling mode, the processes involved are air circulation, air cleaning, cooling and dehumidification. When the system is in heating mode, the processes are heating, circulation, cleaning, and humidification. It should be noted that air circulation is a very important aspect of the total system operation [1].

The main objective of this research is to study the air flow distribution in the library of the Faculty of Engineering. This research was performed using a commercial CFD package known as FLUENT. The air flow dispersal inside the library of faculty of Engineering University Malaya was examined and studied with numerous measures proposed to enhance the results. To achieve this goal, the following tasks were defined:

1) The indoor thermal conditions of ventilated building in a hot humid climate were investigated by using a library as a case-study building type.
2) The indoor thermal conditions and airflow characteristics of the case-study building were analysed by using computer simulations that were calibrated with measured data from the library hall itself.

2. CFD MODELLING

Most of the CFD applications for indoor environment modelling in the last century were to calculate airflow patterns and distributions of air velocity, air temperature, turbulent intensity, and gaseous contaminants, by solving the Reynolds averaged Navier-Stokes equations. More specifically, this study utilised the highly popular [2], standard k-ε eddy-viscosity model.

Nomenclature:

CFD	Computer Fluid Dynamics	UM	University of Malaya
RNG	Renormalization Group	ε	Dissipation (turbulence study)
ρ	Density	t	time
P_k	Generation of turbulence kinetic energy due to the mean velocity gradients	P_b	Generation of turbulence kinetic energy due to buoyancy
C_{nz}	Constant (n = numbers)	S_n	user defined source terms (n = numbers)
k	Turbulence kinetic energy per unit mass	σ_k	turbulent Prandtl number for k
σ_ε	turbulent Prandtl number for ε	T_o	total temperature
T	static temperature	v	velocity

Recently, several studies related to air movement in buildings have been performed using CFD, such as to predict the airflow pattern within a workshop. To compare the results with actual measurements, a combination of CFD model and a reduced-scale physical model was used to simulate the effects of natural ventilation in an open atrium office building [3].

Using CFD, the conservation equations for mass, momentum and thermal energy were solved for all nodes of a two- and three-dimensional grid inside or around the object under investigation. CFD is a relatively new technology, still very much under development. For example, several different CFD solution methods are being investigated for accuracy for airflow simulation inside buildings. These are, direct numerical simulation, large eddy simulation, Reynolds averaged Navier-Stokes modelling, vortex particle method and lattice Boltzmann method [4].

The k-ε model is one of the most common turbulence models in use today. These two variables determine the characteristic length scale of turbulence. In order to achieve an accurate result, a reliable CFD modelling is a must, and it is also essential to adopt a good meshing scheme. A considerable amount of work on choosing a suitable and satisfactory meshing scheme was carried out for this research. Besides that, during the meshing process, various aspects of meshing such as the number of grids and the types of mesh shapes were studied to obtain accurate results [5, 6].

The standard k-epsilon model is a semi-empirical model based on model transport equations for the turbulence kinetic energy, k, and its dissipation rate ε. It is the simplest complete model of turbulence with two partial differential equations in which the solution of two separate transport equations allows the turbulent velocity and length scales to be independently determined. The standard k-epsilon model is therefore, valid only for fully turbulent flows [7].

The two-equation turbulence model of the k-epsilon type was recently derived by using Renormalization Group (RNG) methods for its substantially better predictions than the standard k-epsilon model for turbulence models in separated flows. The improvements obtained from the RNG k-epsilon model were attributed to the better treatment of near wall turbulence effects [8]. The RNG k-epsilon model takes the form below:

For turbulence kinetic energy, k

$$\frac{\partial}{\partial t}(\rho k)+\frac{\partial}{\partial x_i}(\rho k u_i)= \frac{\partial}{\partial x_i}\left[\left(\mu+\frac{\mu_t}{\sigma_k}\right)\frac{\partial k}{\partial x_j}\right]+P_k+P_b-\rho\varepsilon \qquad ...(1)$$

For dissipation, ε

$$\frac{\partial}{\partial t}(\rho\varepsilon)+\frac{\partial}{\partial x_i}(\rho\varepsilon u_i)=\frac{\partial}{\partial x_i}\left[\left(\mu+\frac{\mu_t}{\sigma_\varepsilon}\right)\frac{\partial \varepsilon}{\partial x_j}\right]+C_{1\varepsilon}\frac{\varepsilon}{k}(P_k+C_{3\varepsilon}P_b)-C_{2\varepsilon}\rho\frac{\varepsilon^2}{k}+S_\varepsilon \quad ...(2)$$

3. METHODOLOGY

The locations of the air-conditioning inlets (diffuser) and outlets (return air grille) were identified. The library model simulated has a length of 31.20m, width 25.20m and height of 2.67m. The size of the flow inlet and outlet was 60cm x 60cm. The dimensions of the lights were 120cm x 60 cm as shown in Figure 1.

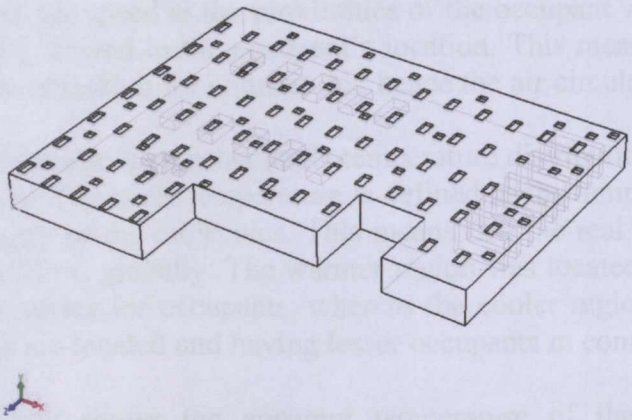

Figure 1: 3D view of Library

SOLIDWORKS was used to define and model the geometry of the library and its boundary conditions. The geometric model was then exported to the pre-processor, GAMBIT version 2.2.30 to carry out meshing of the faces and volumes. Each face of the geometry needs to be meshed appropriately with small interval size so that the problem of skewness does not arise. The elements chosen were TRIs and PAVE for the face meshing. Whereas TET/HYBRID for volume elements and TGRID for volume meshing. Afterwards, the design was then exported into the meshed geometry of FLUENT 6.12.16.

4. RESULTS AND DISCUSSIONS

The room temperature is most favourable to thermal comfort where the occupants of the library do not feel distress, either being too cold or too hot at times. Discomfort exists when occupants do not feel the movement of air at certain places in the library. This can be attributed to the air velocity distribution flowing out from the diffusers.

4.1) Scaled Residuals of Standard K-ε Model

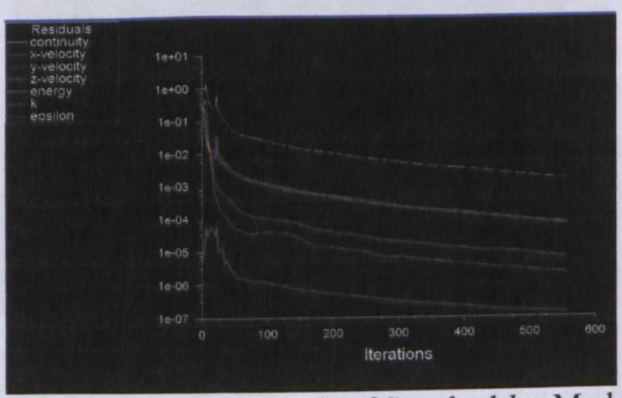

Figure 2: Scaled Residuals of Standard *k*-ε Model

Figure 2 above depicts the scaled residuals of the standard k-ε model. The curves show a converging trend flattening out after 500 iterations. Second order gradients in the mean flow equations and the use of isotropic turbulent viscosity promote numerical stability and ease of calculations in the standard k-epsilon model.

Figure 3(a) below, shows that the air from the inlets was evenly distributed all over the library, with an average value of 0.5m/s, corresponding to the blue region. The maximum velocity magnitude was around 8m/s corresponding to the red region around the return air grille. It can be seen that air speed at the proximities of the occupant was very close to zero, indicating that air hardly flowed to the occupant's location. This means that the system did not provide an optimum condition for comfort and hence the air circulation inside the library area was not optimal.

Figure 3(b) indicates an increasing static temperature distribution moving towards the left portion of the library. The static temperature is defined as the temperature obtained from the average kinetic energy of the molecules. This means that the real temperature of the air was convected with the flow, globally. The warmer region was located at the left side of the library where there are tables for occupants, whereas the cooler region was at the opposite side, where book stacks are located and having lesser occupants in comparison to the warmer region.

Figure 3(c) below shows the apparent temperature of the model as the total temperature. The warmer region falls on the left part of the library model. The regions where occupants sit, are those in the orange, green and light blue regions. The temperature recorded ranged from 20°C to 23°C.

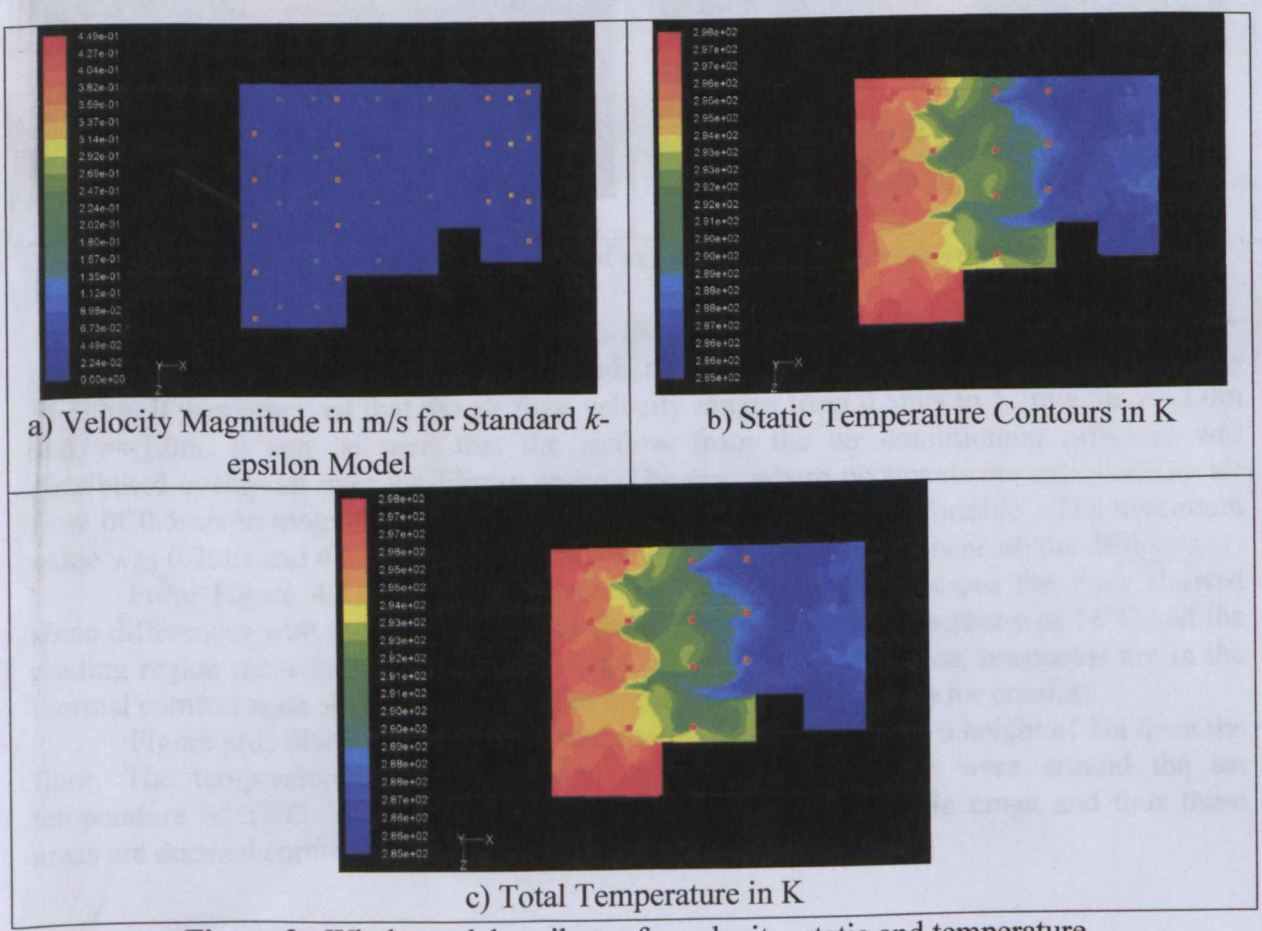

a) Velocity Magnitude in m/s for Standard k-epsilon Model

b) Static Temperature Contours in K

c) Total Temperature in K

Figure 3 : Whole model attributes for velocity, static and temperature

4.2) Contours of Air Flow At Different Iso-Surface

The iso-surfaces for the model were generated and are illustrated below. These surfaces were of constant y-coordinates in which the y-axis plane was being cut. This process was more useful and effective in displaying and conveying the desired results. In this study, the y= -1.0m, y = -2.0m iso-surfaces were generated. These locations of y= -1.0m, y = -2.0m were represented by the height of 1.0m and 2.0m measured from the floor.

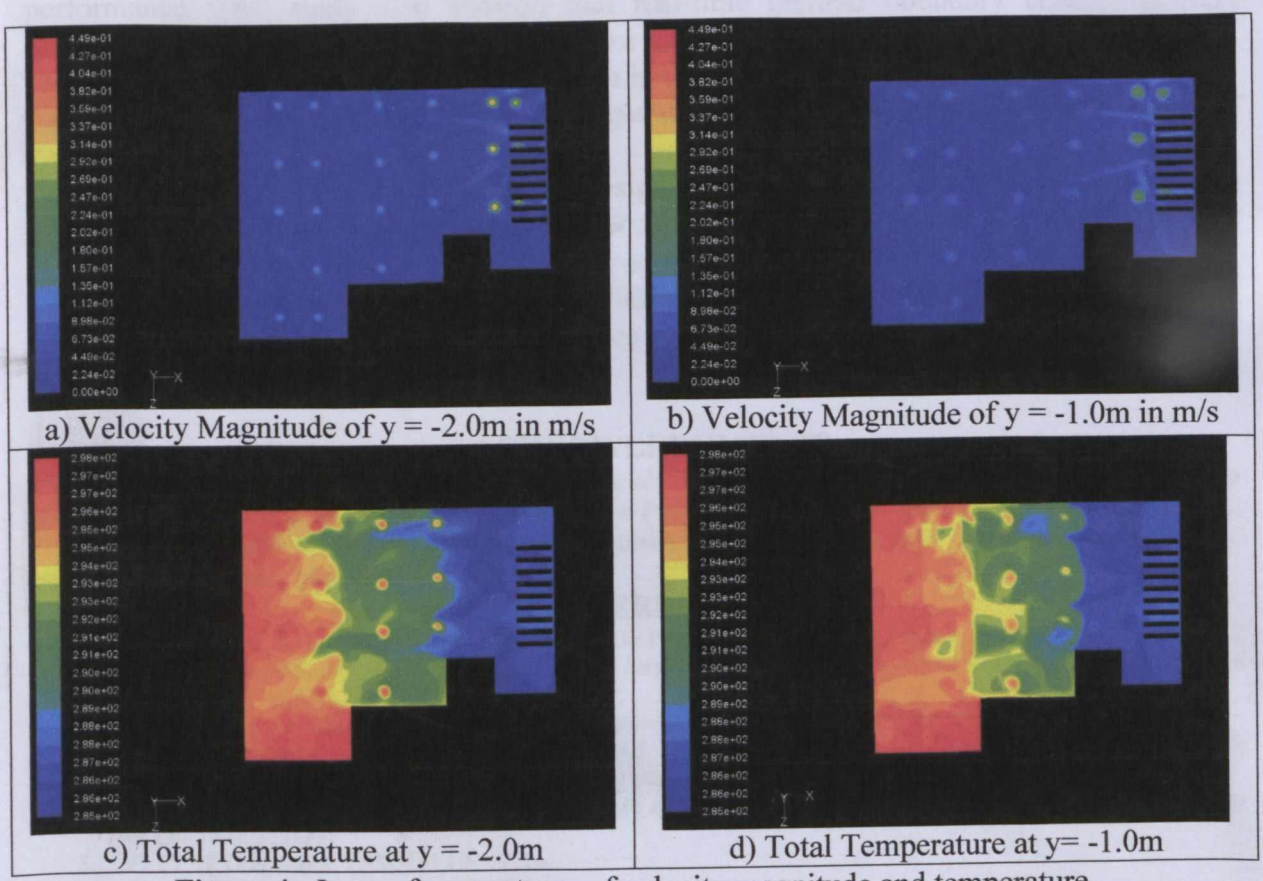

a) Velocity Magnitude of y = -2.0m in m/s

b) Velocity Magnitude of y = -1.0m in m/s

c) Total Temperature at y = -2.0m

d) Total Temperature at y= -1.0m

Figure 4 : Iso-surface contours of velocity magnitude and temperature.

Figure 4(a) and 4(b) above illustrates the air velocity distribution provided by the *k*-ε model with iso-surfaces of velocity magnitude and temperature generated at y = -2.0m and y = -1.0m. It was observed that the air flow velocity ranges from 0.5m/s to 1.2m/s for y=-2.0m and y=-1.0m. It can be seen that the airflow from the air conditioning diffusers was distributed evenly all over the library space. The area where occupants are experiencing air flow of 0.5m/s in magnitude, is quite low for a person to feel comfortable. The maximum value was 6.2m/s and 4.9m/s for y= -2.0m and y=-1.0m respectively, beneath the diffusers.

From Figure 4(c), the total temperature distribution 2.0m above the floor showed some differences with the book stack area recording an average temperature of 16°C and the reading region recording a temperature range of 20°C to 23°C. Hence, occupants are in the thermal comfort zone since the temperature range satisfied the criteria for comfort.

Figure 4(d) illustrate the thermal environment in the library at a height of 1m from the floor. The temperatures in the occupied regions of this library were around the set temperature of 23°C. The temperatures were within the comfortable range and thus these areas are deemed comfortable for the occupants.

5. CONCLUSIONS

This research has investigated the indoor thermal conditions of the library of Faculty of Engineering, University of Malaya. This study has thoroughly analysed the indoor thermal conditions and airflow characteristics of the case-study building. Also, this study has validated CFD results using experimental data obtained from measurements. The validations verified that the program could provide reasonable and reliable predictions on building performance. This study also showed that real-time thermal boundary conditions were important for the accurate assessment of indoor air quality and thermal comfort.

The results obtained from the CFD simulation in this study indicated that:

1) The uniformities of velocity and temperature distributions in the occupied region of the library were satisfactory.
2) For the stratified air-conditioning design in the library building, in order to obtain satisfactory thermal comfort in the occupied region, the mid-height of the building had a good position for the cooling air supply.
3) Analyzing the effects of air-conditioning design parameters on the building environment by CFD was an effective method to find the way to optimize the air-conditioning design scheme.

6. ACKNOWLEDGMENTS

The authors would like to acknowledge the full financial assistance from the Ministry of Science, Technology and Innovation (MOSTI), Malaysia, via e-Science Fund Project 13-02-03-3034 and University of Malaya (UM) PJP Grants FS126/2008B, FS131/2008B and FS219/2008A for research work to be conducted in University of Malaya, Kuala Lumpur, Malaysia.

7. REFERENCES

1. H.J. Steeman, A. Janssens, J. Carmeliet and M. De Paepe.(2009), Modeling Indoor Air and Hygrothermal Wall Interaction in Building Simulation: *Comparison between CFD and a Well-Mixed Zonal Model, Building and Environment*, 44(3), 572-583
2. Launder B. E. and Spading D. B. (1972). *Mathematical Models of Turbulence* (New York: Academic).
3. Atch Sreshthaputra. (2003). *Building Design and Operation for Improving Thermal Comfort in Naturally Ventilated Buildings in A Hot-Humid Climate.* PhD Dissertation. Texas A&M University.
4. Zhiqiang, J.Z. & Qingyan Y.C. (2004). *Performance of coupled building energy and CFD simulations*, University of Colorado. 333-344
5. *FLUENT User Guide.* (2005) FLUENT, Inc.
6. *GAMBIT User Guide.* (2005) FLUENT, Inc.
7. Von Karman, Theodor. (1954), *Aerodynamics, Selected Topics in the Light of Their Theoretical Development.* New York: Cornell University Press.
8. Qingyan(Yan) Chen, Zhao Zhang, and Wangda Zuo (2001), *Computational Fluid Dynamics For Indoor Environment Modeling: Past, Present, And Future,* School of Mechanical Engineering, Purdue University, West Lafayette, USA.
9. Qingyan(Yan) Chen, Zhao Zhang, and Wangda Zuo (2001), Computational Fluid Dynamics For Indoor Environment Modeling: Past, Present, And Future, School of Mechanical Engineering, Purdue University, West Lafayette, USA.
10. ASHRAE, 2001. Handbook 2001 Fundamentals. Atlanta: ASHRAE

METHODOLOGY

Except for the original automobile model, the other five models were mounted with riblets on its body surfaces. The positions identified for investigation are the front of car, the front of roof, the rear of roof, the rear end of car and the side door. For convenience, the five positions hereafter will be referred as Position A, Position B, Position C, Position D and Position E. Each riblet film covers an area of 0.5m x 0.05m as shown in Figure 1. The dimensions of four geometries that are used for investigation about the effect riblets geometry on drag reduction are shown in Figure 2. They are referred to as Geometry A (wedge), Geometry B (square), Geometry C (semi-sphere) and Geometry D (semi-hexagon). All the riblets of different geometry are fixed on Position A. Totally; there are 9 case models to be studied for this project.

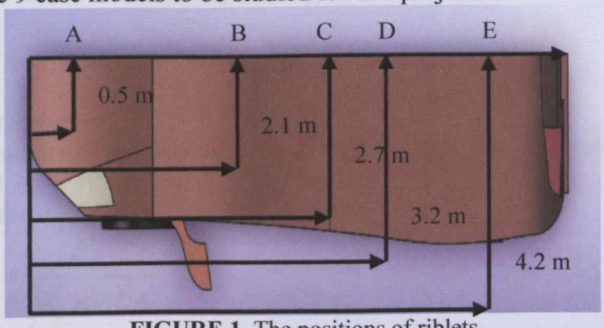

FIGURE 1. The positions of riblets

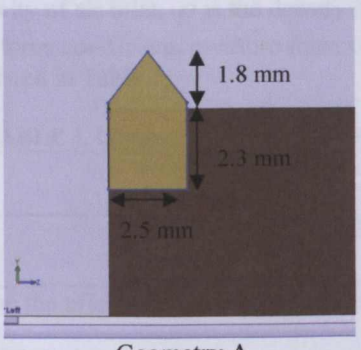

Geometry A

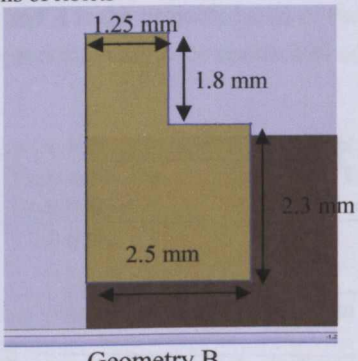

Geometry B

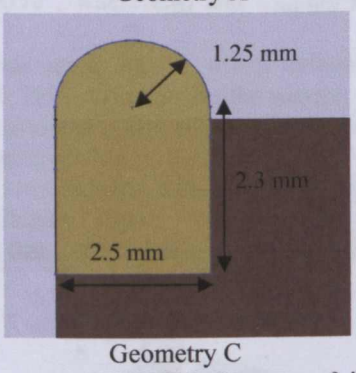

Geometry C

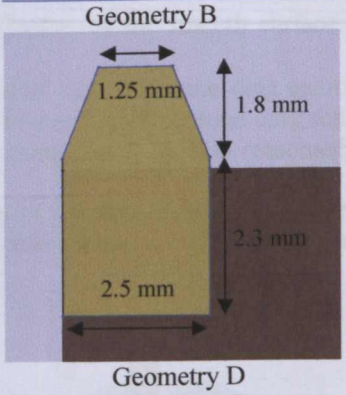

Geometry D

FIGURE 2. Geometry of riblets used: Geometry A, B, C and D.

Velocity inlet

Velocity inlet boundary conditions were used to define the flow velocity, along with all relevant scalar properties of the flow, at flow inlets. This boundary condition is intended for incompressible flows, and its use was appropriate for this case. The inlet velocity was set as $V = 35ms^{-1}$, the approximate to that used in previous experimental works. This value of velocity is also in the range of low speeds (35-45 m/s) which significantly shows the drag reduction by riblets.

Turbulence Specification Method of velocity inlet setting specifies the method to input the turbulence parameters. Turbulence Intensity and Hydraulic Diameter method are chosen because it was assumed that the model was in a virtual wind tunnel where the flow is internally fully developed. For internal flows, the turbulence intensity at the inlets is totally dependent on the upstream history of the flow. If the flow upstream is under-developed and undisturbed, low turbulence intensity can be used. Turbulence intensity is given as $I = 0.16(\mathrm{Re}_{dh})^{-1/8}$. This work simulated the test of the low speed wind tunnel, so the turbulence intensity I is dependent on the parameter of the low speed wind tunnel, I = 0.4% [4]. The hydraulic diameter D_h is selected as another turbulence parameter, D_h = 7.87m.

Outflow

Outflow boundary condition in FLUENT was used to model flow exits where the details of the flow velocity and pressure are not known prior to solution of the flow problem. Outflow was used because this study dealt with an incompressible, steady flow with constant density and the inlet was not a pressure inlet. The outlet condition is that the turbulence is developed sufficiently and the gradient of physical parameter is zero, i.e. $\frac{\partial \psi}{\partial n} = 0$. The outflow boundary was situated far enough downstream from the vehicle so that the outflow conditions have no impact on the flow field in the vicinity of the vehicle.

RESULTS AND DISCUSSION

Effect of Riblets on Drag Reduction

Applying CFD simulations, the viscous force coefficient C_v, and the pressure force, C_p, exerted on the smooth surface models and on a riblet model (Position D, Geometry A) were obtained. The viscous force coefficient and the pressure force coefficient are defined as:

$$C_v = \frac{F_v}{\frac{1}{2}\rho V^2 A} \text{ and } Cp = \frac{F_p}{\frac{1}{2}\rho V^2 A} \quad (1)$$

where V is the velocity of air inlet, ρ is the density of the air, and A is the projected area of the model on the y-z plane. The viscous force coefficient, pressure force coefficient and the total force coefficient of both smooth and riblets models are listed in Table 1.

TABLE 1. Comparison of drag coefficient between smooth surface and riblets model

Model	Pressure force coefficient	Viscous force coefficient	Total force coefficient
Smooth surface	0.3355	0.0262	0.3617
Riblets	0.3314	0.0203	0.3518

To examine the effect of the riblets model on total drag reduction, the drag reduction rate is defined as $\frac{C_{SM} - C_{RM}}{C_{SM}} \times 100\%$, where C_{SM} and C_{RM} are drag coefficients of the smooth surface model and riblets model. The reduction rate is 2.74%, which indicates that riblets can reduce the drag exerting on automobile under low air speed. This result verifies the solving approach of this study, since the drag reduction by riblets is proven in various researches. The values of drag coefficient simulated, 0.36, also reasonably close to the real Lamborghini Murcielago LP640's 0.33.

Table 1 shows that for both models, the major part of the drag coefficient is attributed to pressure viscous force coefficient (Figure 3). It was also observed that riblets are more efficient on viscous drag reduction (22.52%) than pressure drag reduction (1.22%).

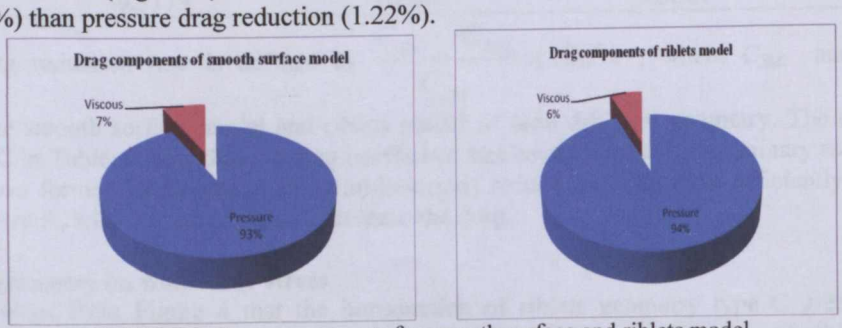

FIGURE 3. Drag components for smooth surface and riblets model.

The values of pressure and viscous drag force for both models are shown in Table 2. The drag force reduction rate was calculated as its drag coefficient counterpart, and found to be 2.6%. Both rates are quite close, and according to Equation 1, the drag coefficient and drag force are proportional to each other. Hence, the subsequent discussion will focus on the drag coefficient parameter only.

TABLE 2. Comparison of drag force between smooth surface and riblets model

Model	Pressure force (N)	Viscous force (N)	Total force (N)
Smooth surface	418.03	32.66	450.68
Riblets	411.00	27.96	438.96

Effect of Riblets Position on Drag Reduction

The previous results have proven that riblets could reduce the drag of a vehicle, and the solving model of this study has been verified. The second part of the discussion will focus on how the different locations of riblets to be placed have influenced the drag reduction. Five positions has been identified and used for this investigation. The results of simulation of each model are tabulated below:

TABLE 3. Comparison of drag coefficient and reduction rate of different positioned riblets.

MODEL	PRESSURE FORCE COEFFICIENT	VISCOUS FORCE COEFFICIENT	TOTAL FORCE COEFFICIENT	REDUCTION RATE (%)
Smooth	0.3355	0.0262	0.3617	-
Position A	0.3398	0.0201	0.3599	0.50
Position B	0.3149	0.0207	0.3356	7.22
Position C	0.3054	0.0219	0.3273	9.51
Position D	0.3314	0.0203	0.3518	2.74
Position E	0.3224	0.0210	0.3434	5.06

The drag reduction rate is defined as $\frac{C_{SM} - C_{RM}}{C_{SM}} \times 100\%$, where C_{SM} and C_{RM} are drag coefficients of the smooth surface model and riblets model of each different position. The positions, from A to E, are shown in Figure 1above. Relating the location of these positions with the calculated reduction rate, it is observed that the reduction rate is the lowest near the front of the car, increasing until the mid of the car (position E), and finally fluctuating from A to D. It is interesting to note that apparently there is no proportionality occurs between these positions and the reduction rate, thus a further analysis is required to find out their relationship.

Effect of Riblets Geometry on Drag Reduction

For this section, various riblet geometries are simulated to investigate its performance on drag reduction. Four geometries are chosen, referred as Geometry A (wedge), Geometry B (square), Geometry C (semi-sphere) and Geometry D (semi-hexagon).

TABLE 4. Reduction rates of different riblet geometries

Model	Pressure Force Coefficient	Viscous Force Coefficient	Total Force Coefficient	Reduction Rate (%)
Smooth	0.3355	0.0262	0.3617	-
Geometry A	0.3314	0.0203	0.3518	2.74
Geometry B	0.3481	0.0205	0.3686	-1.91
Geometry C	0.3533	0.0205	0.3738	-3.34
Geometry D	0.3179	0.0207	0.3387	6.36

The drag reduction rate is defined as $\frac{C_{SM} - C_{RM}}{C_{SM}} \times 100\%$, where C_{SM} and C_{RM} are drag coefficients of the smooth surface model and riblets model of each different geometry. The reduction rates of geometry B and C in Table 4 show that the drag coefficient has been increased. Preliminary result indicates that the sharp V-groove formed by Geometry D (semi-hexagon) reduce the drag most efficiently, followed by V-groove of Geometry A, while B and C slightly increase the drag.

Effect of riblet geometry on wall shear stress

It is obvious from Figure 4 that the introduction of riblets geometry type C greatly increases the turbulent wall shear stress, to a level approaching 8.5 Pa. While the other 3 types of riblets are steady in maintaining shear stress in range 0.5-5 Pa, with the most efficient by geometry D, followed by B then A.

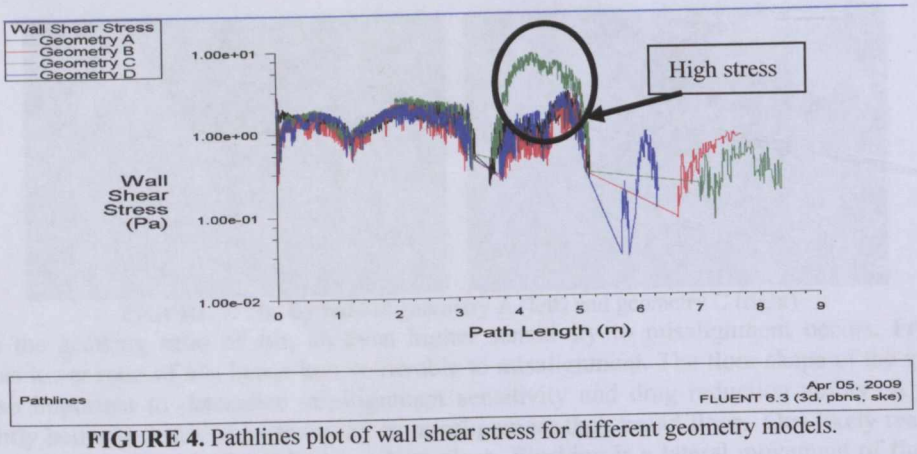

FIGURE 4. Pathlines plot of wall shear stress for different geometry models.

Hampering the velocity in lateral direction will reduce momentum transfer and skin friction, such that align the riblets in the mean flow direction. Second, the protrusions should not higher than $y^+ \approx 5$, which will increase the drag. Third, the protrusion height difference, Δh is required to be maximized for higher drag reduction.

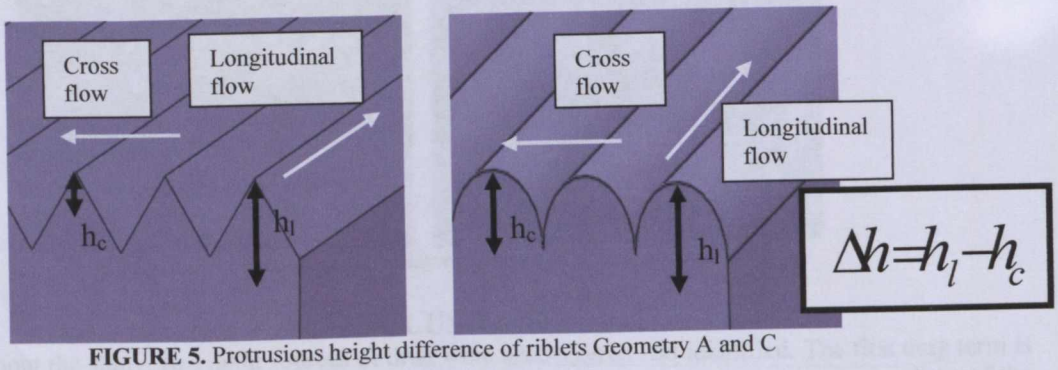

FIGURE 5. Protrusions height difference of riblets Geometry A and C

From the 3 factors above, all the 4 geometries of riblets do reduce airflow speed and have the riblets height from 1.25 mm to 1.8 mm, with y^+ of C lower than A in this comparison. The only factor differentiate them is the protrusion height. When experiencing cross flow, the virtual origin of geometry C cannot remains near to tips due to its sphere shape, results in higher h_c, hence its drag reduction function deteriorates.

Riblet geometry and misalignment vulnerability

It is important to understand the deteriorating effect of misalignment because deviations in flow direction do occur at varying angle of attack of the surface. Three geometric quantities are responsible for the sensitivity to misalignment: the rib lateral spacing, s^+, the ratio of rib height to rib spacing, h/s, and the shape of the cross section valley between two ribs.

The spacing of riblets in different geometries used in this study is the same, that is 2.5 mm. For a given ratio of h/s = 0.5, the trapezoidally grooved riblets with smaller groove angle will perform better. Comparing the two trapezoidally and triangularly grooved of the study models here, the groove angle of geometry D is smaller, hence it is believed that it has the advantage in this prospect.

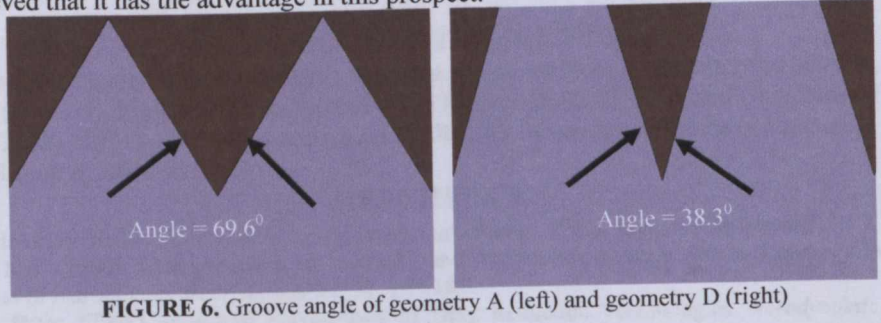

FIGURE 6. Groove angle of geometry A (left) and geometry D (right)

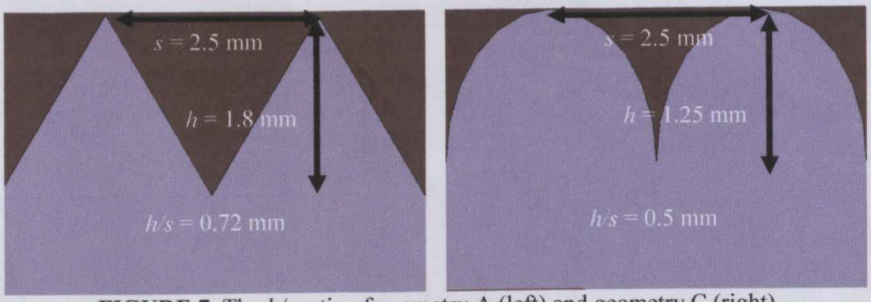

FIGURE 7. The *h/s* ratio of geometry A (left) and geometry C (right)

With the growing ratio of *h/s*, an even higher sensitivity to misalignment occurs. From Figure 7, geometry C has lower ratio of *h/s*, hence less vulnerable to misalignment. The floor shape of the valley between the ribs is also important to determine misalignment sensitivity and drag reduction ability. A narrow notch performs slightly better in terms of insensitivity to misalignment than broad floor. One likely reason for this is the phenomenon that the fluid in the valleys tends to slosh. Sloshing is a lateral movement of fluid in between the ribs, which produces a motion normal to the wall. This additional momentum exchange is responsible for additional losses in drag reduction, and its appearance is more likely for broader valleys, such as the one formed by geometry B.

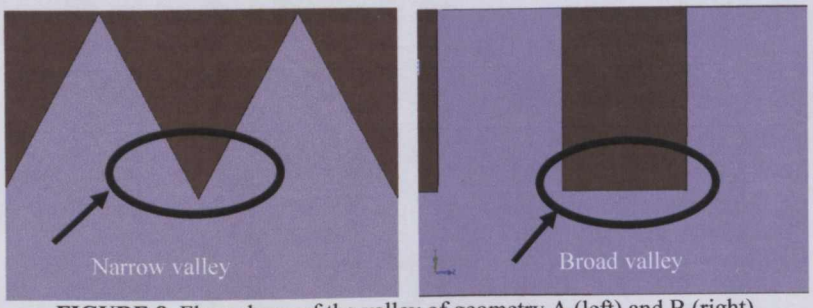

FIGURE 8. Floor shape of the valley of geometry A (left) and B (right).

CONCLUSIONS

Throughout the study, two main sources of drag were encountered and identified. The first drag term is called the form drag, which is also referred to as pressure drag, caused by the adverse pressure gradient of the flow domain around the automobile. The second source of drag is the friction drag, caused by the wall shear stress of the air flow through the surface of the automobile. Using the wedge shape riblets with a triangular cross-section attached on the rear roof of the automobile, the effect of the riblets has been studied. The drag coefficient of a smooth surface model is simulated to be 0.3617, while the use of wedge riblets was found to have drag reduction rate of 2.74%. The position of riblets attached on top of the middle roof of the automobile was found to be the most ideal, as far as drag reduction is concerned. A reduction rate as high as 9.51% was recorded for this position, while several more positions were investigated and the corresponding reduction rate falls in the range of 0.5-7.22%. The riblets on middle roof (referred as position C) is discovered to have better performance on reducing pressure gradient, vorticity and turbulence intensity, inducing lower wall shear stress, restricts the airflow speed and less susceptible to yaw angle effect. Among the four geometries of riblets investigated, the semi-hexagon trapezoidally shaped riblets, with narrow V-grooves (geometry D), was found to be the best. A drag reduction rate of 6.36% was obtained from this geometry, while the semi-circular and square cross section geometries reported to have increased the drag.

ACKNOWLEDGMENTS

The authors would like to acknowledge the full financial assistance from the Ministry of Science, Technology and Innovation (MOSTI), Malaysia, via e-Science Fund Project 13-02-03-3034 and University of Malaya (UM) PJP Grants FS126/2008B, FS131/2008B and FS219/2008A for research work to be conducted in University of Malaya, Kuala Lumpur, Malaysia.

REFERENCES

1. Wolf-Heinrich Hucho. (1997). *Aerodynamics of road vehicles*. 4th Ed. London: Butterworth.
2. Walsh M.J. (1980). Drag reduction of V-groove and transverse curvature riblets. *Viscous flow drag reduction, Progress in Astronautics and Aeronautics*. **72**. 168-184.
3. Thiede Peter. (2001). Industrial Perspectives of Drag Reduction Technologies. *Aerodynamic Drag Reduction Technologies: Proceedings of the CEAS/DragNet European Drag Reduction Conference, 19-21 June 2000, Potsdam, Germany*. **76**. 259-266. /
4. Tian L.R., Red L.Q., Lid Q.P., Had Z.W., Xiao Jiang. (2007). The Mechanism of Drag Reduction around Bodies of Revolution Using Bionic Non-Smooth Surfaces. *Journal of Bionic Engineering*. **4**. 109-116.